ACS APPLIED NANO MATERIALS

www.acsanm.org Article

Mesoporous ZnS-Sb/C Reduced Graphene Oxide Nanostructures as Anode Materials for Sodium-Ion Batteries

Ming Zhu, Yi Jiang, Xijia Yang, Xuesong Li, Liying Wang,* and Wei Lü*

Cite This: *ACS Appl. Nano Mater.* 2023, 6, 13503−13512 Read Online

ACCESS | Metrics & More | Article Recommendations | Supporting Information

ABSTRACT: Metal-based sulfides are favored by researchers because of their high theoretical capacity, but their inherent volume expansion problems limit their further applications. To address the above issues, we prepared ZnS-Sb@C@rGO core−shell nanosphere anode materials for high-performance sodium-ion batteries (SIBs). The ZnS-Sb heteromeric core with synergistic effects was designed to facilitate rapid electrolyte penetration and accelerate Na^+ transformation kinetics. Meanwhile, the double coating of the outer carbon shell and rGO layer provides rich sodium embedding sites and improves the conductivity and charge transfer capability of the composite. Its unique layered heterogeneous structure design provides a lot of buffer space and effectively prevents the shedding of active substances. The composite has excellent electrochemical properties in sodium-ion batteries, with a high initial discharge specific capacity of 1117.1 mAh g^{-1} at 0.1 A g^{-1}. The battery achieves a long cycle life, and the discharge specific capacity is 210.3 mAh g^{-1} after 300 cycles at 1 A g^{-1}. This novel structural design may be one of the feasible solutions to achieve the excellent properties of SIB anode materials.

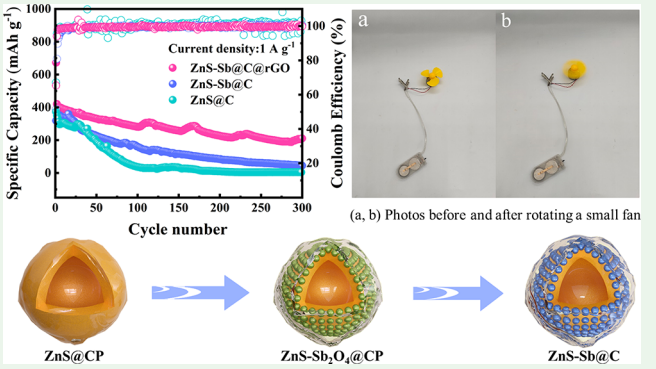

KEYWORDS: *pseudocapacitance, Coulombic efficiency, heterostructure, electrochemical impedance, capacity retention*

1. INTRODUCTION

Lithium-ion batteries (LIBs) have been broadly used in 3C consumer electronics, renewable energy storage, and other fields.[1−4] However, two factors limit the further development of LIBs. One reason is that lithium has limited resources, uneven distribution, and high cost, which limits the large-scale application of lithium.[5,6] The other is that commercial LIBs use a single graphite anode, whose structural features hinder the further improvements in cycling and rate performance.[7,8] Due to the similar nature of sodium-ion batteries (SIBs) and LIBs and the richer resources of SIBs, SIBs are expected to replace LIBs to solve the large-scale energy storage problem.[9−12] Improving a novel anode material with novel shape and controllable composition can further enhance the sodium storage performance.

Recently, metal-based sulfides, metal-based materials, and carbon-based materials have received increasing attention as SIB anode materials.[13−19] Among them, the theoretical capacity of metal sulfides (such as ZnS, Sb_2S_3, NiS, etc.) are particularly prominent, which have been studied by researchers.[20−22] Zhang et al.[23] prepared ZnS nanofibers by a template method and obtained an initial reversible capacity of 603 mAh g^{-1} at 100 mA g^{-1}. Jin et al.[24] synthesized Sb_2S_3 nanowires by a one-step hydrothermal method, and SIBs based on Sb_2S_3 nanowires achieved high-capacity retention rates in long-term cycle. Compared with Sb_2S_3, the element Sb has better electrical conductivity and chemical stability.[21,25,26] Hou et al.[27] prepared a Sb porous microsphere by a displacement reaction, and the porous Sb microsphere prepared by this method showed significant capacity retention. However, both metal-based sulfides and metal-based materials, due to their inherent volume expansion problems, may lead to the crushing or shedding of active substances, resulting in a sharp decrease in cycling capacity.[28−30] To address this issue, researchers usually add carbon-based materials or build unique nanostructure frameworks. For example, Wang et al.[31] synthesized ZnS/NC nanoparticles and achieved excellent electrochemical properties in the SIB anode. Yang et al.[32] reported a novel A-Sb/NC mixture with a specific capacity of 280.5 mAh g^{-1} after 500 cycles at 1 A g^{-1}. Therefore, combining carbon materials and constructing unique nanostructures have been shown to be viable solutions for improving the SIB volume expansion.

Received: May 15, 2023
Accepted: July 10, 2023
Published: July 20, 2023

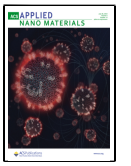

https://doi.org/10.1021/acsanm.3c02158
ACS Appl. Nano Mater. 2023, 6, 13503−13512

In this paper, we designed ZnS-Sb@C@rGO core−shell nanospheres as anodes for high-performance SIBs. The precursor of the carbon polysaccharide ZnS@CP was synthesized by a hydrothermal method, and part of the Zn in ZnS was replaced by Sb in an antimony source. After oxidation in air, carbonization, and graphene coating treatment, ZnS-Sb@C@rGO core−shell nanospheres were obtained. The ZnS-Sb heterogeneous core can accelerate the electron migration at the inside interface of the two materials and improve the interface response dynamics of the material. At the same time, the external carbon layer and rGO layer can improve the electrical conductivity of the working electrode, provide a huge buffer for the composite, prevent the collapse of the material structure, and ensure the structural stability of the composite material. This novel layered design increases the contact area between the electrolyte and the active material, greatly shortens the Na^+ diffusion path, and improves the transfer kinetics of the composite. Scanning electron microscope (SEM) images after subsequent circulation showed that the synergistic effect of the ZnS-Sb core and outer double carbon layer can effectively improve the pulverization and collapse of electrode materials, and the synthetic ZnS-Sb@C@rGO core−shell nanospheres have excellent structural durability.

2. EXPERIMENTS

2.1. Synthesis of ZnS@CP. Zinc acetate (6 mmol), thioacetamide (12 mmol), polyvinyl pyrrolidone (0.5 g, PVP-K30), and glucose (0.5 g) had been sequentially introduced to a 60 mL combined solution (deionized water:ethanol = 1:1). The above mixture was subjected to ultrasound for half an hour to evenly disperse it. Then, it was transferred to a 180 °C blast drying oven for insulation for 14 h. After cooling and centrifugal washing, we obtained a ZnS@CP carbonaceous polysaccharide precursor.

2.2. Synthesis of ZnS-Sb_2O_4@CP. The ZnS@CP precursor (0.5 g), potassium antimony tartrate (5 g), and tartaric acid (1.5 g) were sequentially added to 100 mL of water solution and stirred vigorously at 90 °C for 24 h. After the reaction, the ZnS-Sb_2O_4@CP intermediate product was obtained by centrifugation and washing.

2.3. Synthesis of ZnS-Sb_2O_4@CP@rGO. ZnS-Sb_2O_4@CP (0.3 g) was added to 25 mL of graphene oxide (GO) aqueous solution. After stirring vigorously for 2 h, it was transferred to a freeze dryer for 24 h. After the reaction, the ZnS-Sb_2O_4@CP@rGO sample was obtained.

2.4. Synthesis of ZnS-Sb@C@rGO. A 3 g ZnS-Sb_2O_4@CP@rGO sample was annealed in a tubular furnace at 530 °C for 2 h, and a ZnS-Sb@C@rGO composite was obtained after carbonization. In addition, the ZnS@CP precursor was annealed to obtain ZnS@C, and the ZnS-Sb_2O_4@CP intermediate product was annealed to obtain a ZnS-Sb@C composite by the same process. The obtained ZnS@C and ZnS-Sb@C products were used as control samples in this experiment.

3. RESULTS AND DISCUSSION

Figure 1 shows the preparation process of ZnS-Sb@C@rGO composites. First, the carbon-containing polysaccharide precursor ZnS@CP was synthesized by the hydrothermal method. Through the cation exchange method, the Sb in the antimony potassium tartrate was partially replaced by Zn to form Sb_2S_3, with was further oxidized to form Sb_2O_4 during the oil bath, resulting in the intermediate ZnS-Sb_2O_4@CP. The surface of the ZnS-Sb_2O_4@CP was covered by GO through stirring and ultrasonic treatment, and the GO showed a loose and porous structure after freeze-drying. Finally, the ZnS-Sb_2O_4@CP@rGO samples were annealed in a nitrogen

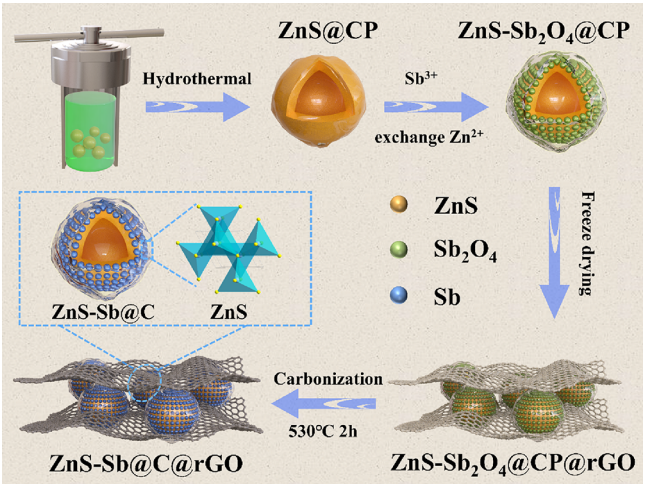

Figure 1. Schematic diagram of the ZnS-Sb@C@rGO composite.

atmosphere with CP as a reducing agent to reduce Sb_2O_4 to Sb and CP itself into a carbon layer and coated on the outer layer of mesoporous nanospheres. After annealing, the rGO was coated in the outermost layer to form the ZnS-Sb@C@rGO core−shell nanospheres with a carbon layer and rGO layer.

The microscopic morphology of ZnS@C, ZnS-Sb_2O_4@CP, ZnS-Sb@C, and ZnS-Sb@C@rGO were observed by SEM. ZnS@C is the form of nanospheres stacked on each other with a particle size between 500 nm and 1000 nm (Figure 2a and Figure S1a,b). After annealing at high temperatures, the polysaccharide polymer CP is converted into an amorphous carbon layer with a rough surface and large amounts of mesopores on the nanospheres. The SEM images of ZnS-Sb_2O_4@CP are shown in Figure 2b and Figure S1c,d, which are similar to the morphology of ZnS@C and also appear as

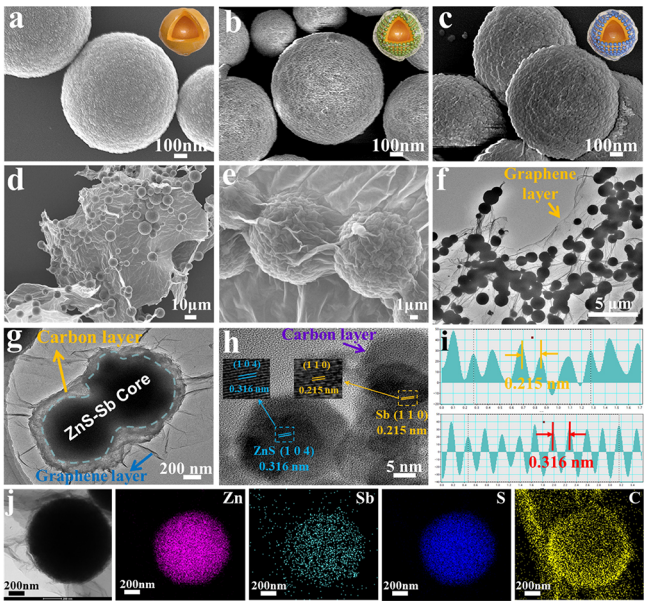

Figure 2. (a−c) SEM images of ZnS@C, ZnS-Sb_2O_4@CP, and ZnS-Sb@C. (d, e) Different magnification SEM images of ZnS-Sb@C@rGO. (f, g) TEM images of ZnS-Sb@C@rGO. (h) HRTEM image of ZnS-Sb@C@rGO. (i) Lattice fringe spacing measurement map. (j) Elemental mapping of ZnS-Sb@C@rGO.

https://doi.org/10.1021/acsanm.3c02158
ACS Appl. Nano Mater. 2023, 6, 13503−13512

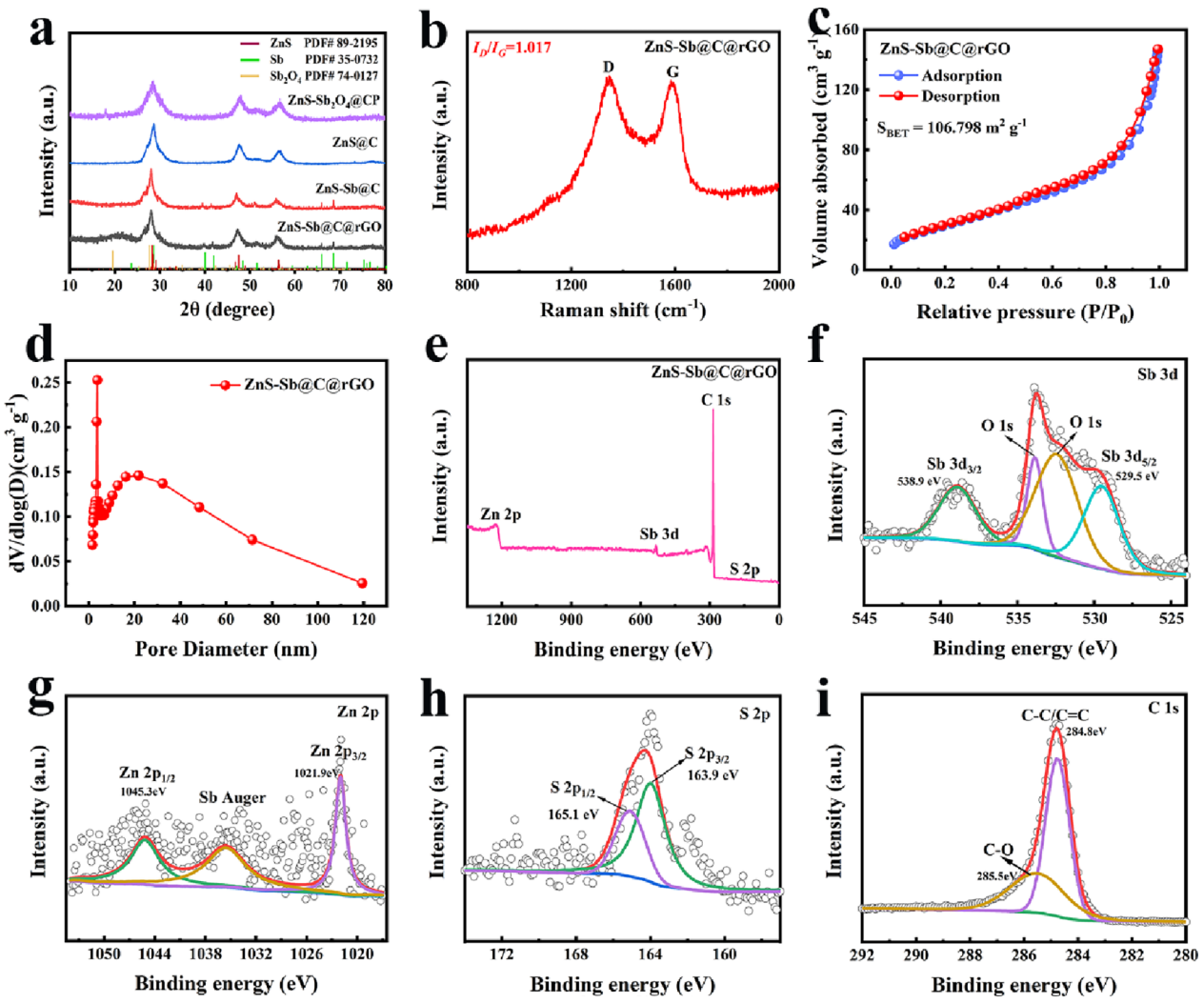

Figure 3. (a) XRD images of the four materials. (b) Raman spectra of ZnS-Sb@C@rGO. (c) N_2 adsorption/desorption isotherm of ZnS-Sb@C@rGO. (d) Pore size distribution of ZnS-Sb@C@rGO. (e) XPS survey spectra of ZnS-Sb@C@rGO. (f–i) High-resolution Sb 3d, Zn 2p, S 2p, and C 1s XPS spectra of ZnS-Sb@C@rGO.

nanospheres of a similar size. The ZnS-Sb_2O_4@CP nanospheres are not annealed at high temperatures and show poor crystallinity and low surface roughness. In Figure 2c and Figure S1e,f, ZnS-Sb@C nanospheres show significant surface roughness. After high-temperature annealing, Sb_2O_4 is reduced to a more stable elemental Sb, and CP is transformed into an uncertain carbon layer and cover the outer layer of the nanospheres. The synergistic interaction of the carbon layer with ZnS-Sb provides the good cyclic stability of SIBs.

In Figure 2d,e, the SEM images of ZnS-Sb@C@rGO show 500−1000 nm nanosphere shapes with each nanosphere evenly embedded in the rGO layer with a folded surface, providing more sodium insertion sites and electrolyte/electrode contact area. Figure 2f,g and Figure S2b show the TEM images of ZnS-Sb@C@rGO, which can be seen in the form of core−shell nanospheres, and a layer of rGO network is clearly observed on the surface. The introduction of rGO with high toughness and high ductility effectively alleviates the huge volume expansion during charge and discharge and further improves the cyclic stability of the composites. Figure 2h shows the HRTEM image. It can be seen that there is an amorphous carbon layer on the ZnS-Sb surface of the ZnS-Sb@C@rGO core−shell nanospheres.

In Figure 2i and Figure S2a, 10 peaks are selected to measure the average value, a lattice constant of 0.316 nm is related to the (104) crystal face of ZnS (PDF#89-2195), and that of 0.215 nm correlates to the (110) crystal face of Sb (PDF#35-0732). The clear boundary between the two proves the formation of hybrid heterostructures of ZnS and Sb. The uniform distribution of Zn, Sb, S, and C elements in the composite proves the successful synthesis of the ZnS-Sb@C@rGO composite (Figure 2j). In Figure S3, the EDX results of ZnS-Sb-C@rGO composites further confirm the existence of all Zn, S, Sb, and C elements, where the atomic ratios of Zn, Sb, S, and C are 59.61, 1.3, 15.07, and 24%, respectively. In Figure S4, the carbon content of ZnS-Sb@C@rGO composites was evaluated by thermogravimetric analysis (TGA). The weight loss from room temperature to 750 °C is mainly related to the oxidation of carbon and graphene, and the carbon content of the composite is 16.4%.

In Figure 3a, the crystal structures of ZnS@C, ZnS-Sb_2O_4@CP, ZnS-Sb@C, and ZnS-Sb@C@rGO were analyzed by X-ray diffractometry (XRD). There are three distinct strong peaks in all four materials, corresponding to the (104), (110), and (205) crystal planes of ZnS (PDF#89-2195), respectively. ZnS-Sb@C and ZnS-Sb@C@rGO diffraction peaks can be

https://doi.org/10.1021/acsanm.3c02158
ACS Appl. Nano Mater. 2023, 6, 13503−13512

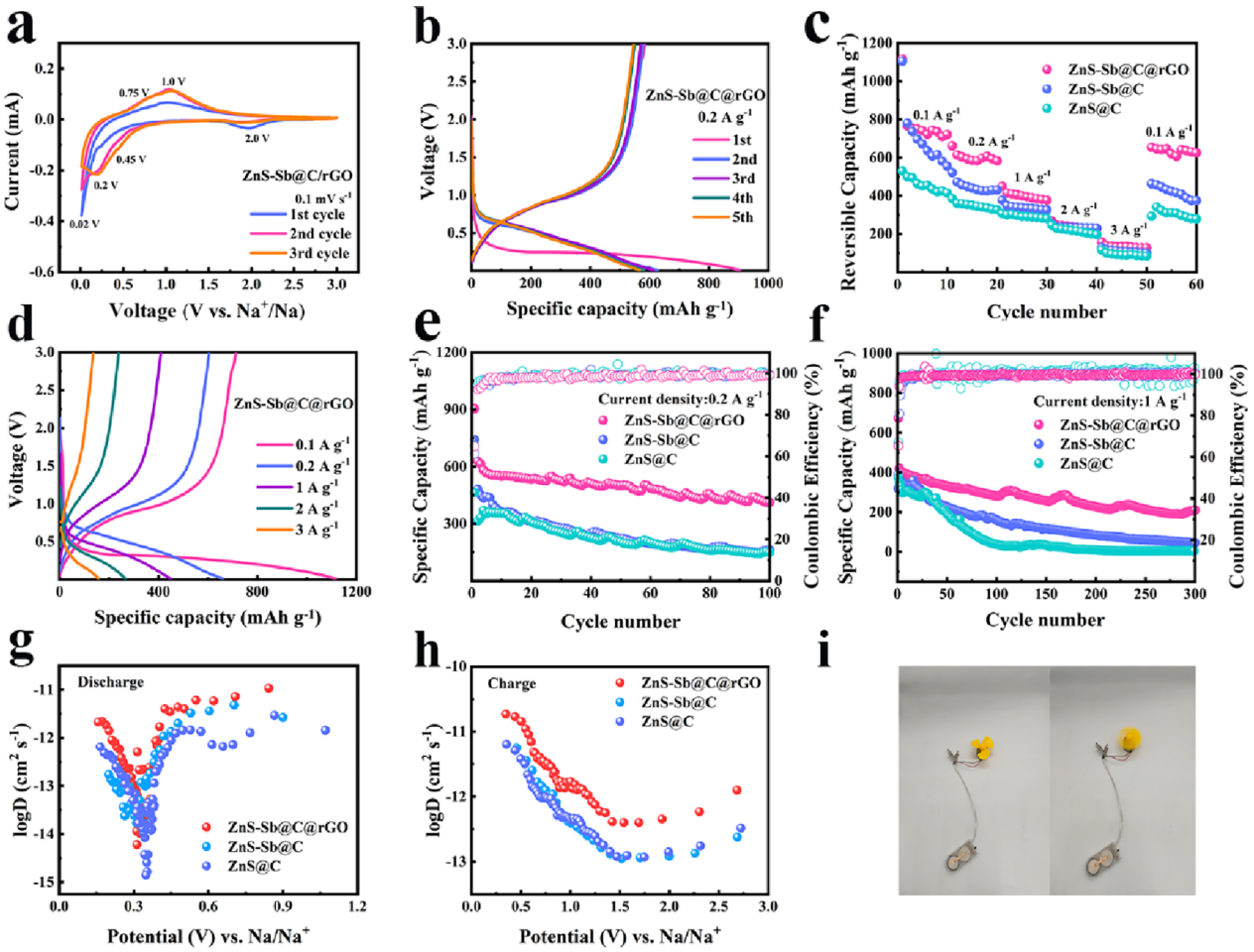

Figure 4. (a) CV curves of ZnS-Sb@C@rGO at 0.1 mV s^{-1}. (b) GCD curves of ZnS-Sb@C@rGO at 0.2 A g^{-1}. (c) Rate capability of ZnS@C, ZnS-Sb@C, and ZnS-Sb@C@rGO at different current densities. (d) GCD curves of ZnS-Sb@C@rGO at different current densities. (e) Cycling performance of ZnS-Sb@C@rGO, ZnS-Sb@C, and ZnS@C at 0.2 A g^{-1}. (f) Cycling stability of ZnS-Sb@C@rGO, ZnS-Sb@C, and ZnS@C anodes at 1 A g^{-1} for 300 cycles. (g, h) Corresponding diffusion coefficients during sodification and desodification. (i) Photos before and after rotating a small fan using ZnS-Sb@C@rGO electrodes.

observed at 28.6, 40.1, 41.9, 65.9, and 68.5°, which are consistent with the (012), (104), (110), (116), and (122) crystal planes of Sb metal (PDF#35-0732); it is confirmed that the composite materials contain the Sb element. In the XRD pattern of ZnS-Sb_2O_4@CP, the peaks at 17.9 and 29.0° are listed to the (011) and (112) crystal planes of Sb_2O_4, indicating that Sb exists in the shape of oxides in the ZnS-Sb_2O_4@CP electrode. Figure 3b exhibits the Raman spectrum of ZnS-Sb@C@rGO. The two peaks at 1346 and 1584 cm^{-1} coincide to the D and G bands, respectively, and the peak intensity ratio (ID/IG = 1.017) is higher than that of the control sample ZnS-Sb@C (Figure S4, ID/IG = 0.919); the degree of graphitization is higher, indicating that the graphene and carbon layers have fewer lattice defects.[33,34] In Figure 3c, the specific surface area of the ZnS-Sb@C@rGO sample is 106.798 m^2 g^{-1} by the BET method. As exhibited in Figure 3d, there are plentiful mesopores in ZnS-Sb@C@rGO with an average pore measurement of 7.4 nm. The large specific surface area and abundant mesopores of the ZnS-Sb@C@rGO sample provide a great number of Na^+ intercalation sites, which facilitate electrolyte permeation and enhance Na^+ transfer kinetics.

To study the elemental chemical states of ZnS-Sb@C@rGO composites, XPS characterization was performed. Figure 3e shows the total XPS spectrum of ZnS-Sb@C@rGO, in which diffraction peaks of Zn, S, Sb, and C are detected, confirming the existence of the above elements. In Figure 3f, the high-resolution XPS image of Sb 3d shows that the peaks at 529.5 and 538.9 eV coincide to Sb $3d_{5/2}$ and Sb $3d_{3/2}$, respectively.[35] O 1s contains two peaks at 533.9 and 532.9 eV, which may be part of the oxygen absorbed by the sample exposed to air.[36,37] Two peaks appear at 1045.3 and 1021.9 eV in Figure 3g, which are related with Zn $2p_{3/2}$ and Zn $2p_{1/2}$ orbitals, proving the presence of Zn^{2+}.[38] In Figure 3h, the peaks at 163.9 and 165.1 eV belong to S $2p_{3/2}$ and S $2p_{1/2}$, indicating the presence of S^{2-} in the sample.[39] In Figure 3i, the two peaks at 285.5 and 284.8 eV belong to C−O and C−C/C═C bonds, respectively, confirming the presence of graphene and amorphous carbon layers in the composite.[40,41]

The working mechanism of the ZnS-Sb@C@rGO sample was analyzed by cyclic voltammetry. Figure 4a gives the CV curves of ZnS-Sb@C@rGO at a voltage window of 0−3 V. It can be seen that during the first cycle of discharge, the first broad peak of ZnS-Sb@C@rGO will appear at around 2.0 V, which belongs to the process of forming a solid electrolyte interfacial (SEI) film.[42] The weak peak that appeared at 0.45 V is attributed to the process of alloying to generate Na_3Sb.[43] The two peaks at 0.2 and 0.02 V are the alloying procedure to

https://doi.org/10.1021/acsanm.3c02158
ACS Appl. Nano Mater. 2023, 6, 13503−13512

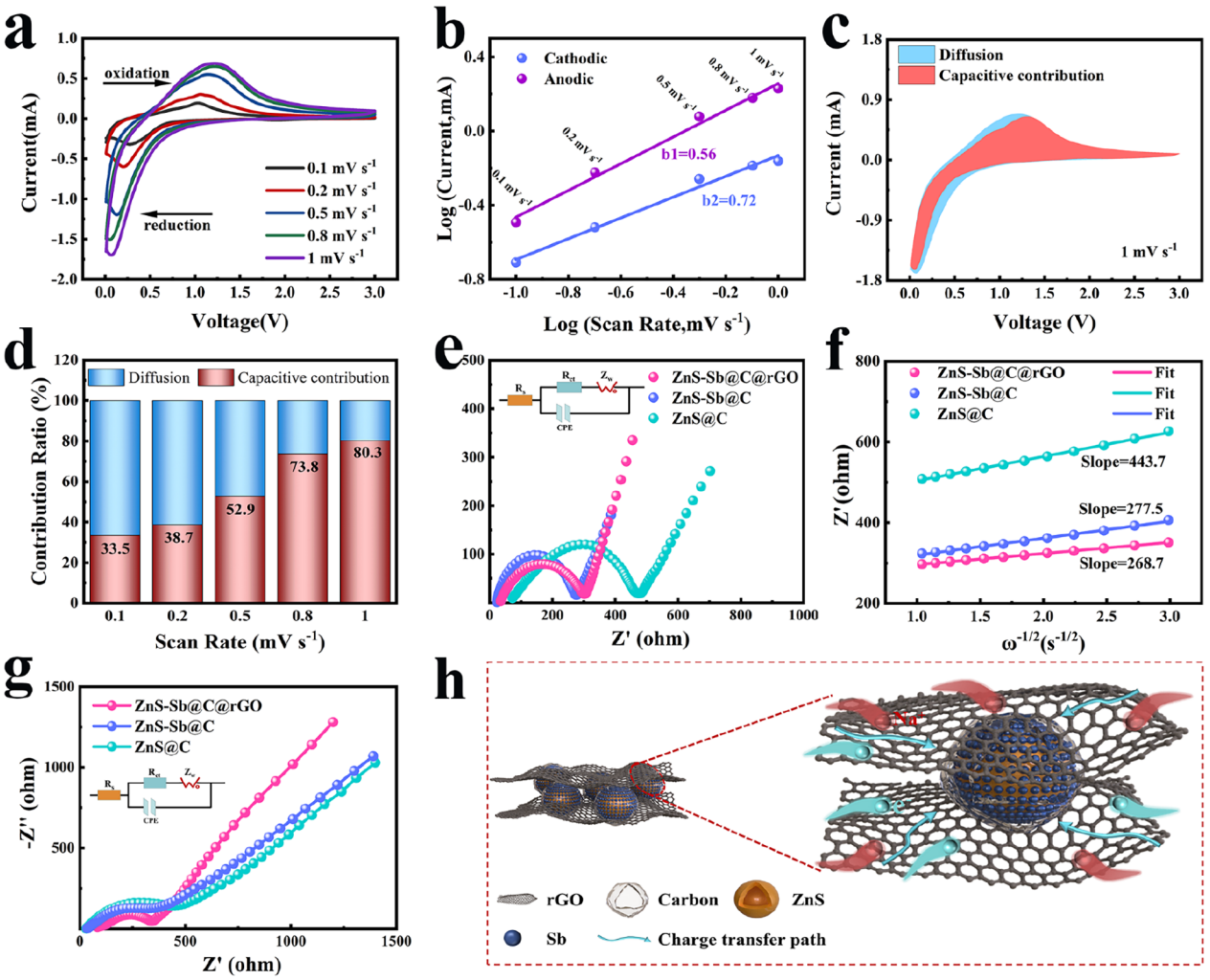

Figure 5. (a) CV curves of ZnS-Sb@C@rGO at different scanning speeds. (b) Cathodic peak and anodic peak log(v) and log(i) fitting graph. (c) ZnS-Sb@C@rGO pseudocapacitance ratio at 1 mV s^{-1}. (d) ZnS-Sb@C@rGO pseudocapacitance and diffusion ratio at different scanning speeds. (e) EIS spectra of ZnS@C, ZnS-Sb@C, and ZnS-Sb@C@rGO. (f) Linear fitting of Z' and $\omega^{-1/2}$ for ZnS@C, ZnS-Sb@C, and ZnS-Sb@C@rGO. (g) EIS spectra of ZnS@C, ZnS-Sb@C, and ZnS-Sb@C@rGO after 100 cycles at 0.2 A g^{-1}. (h) Diagram of sodification and desodification characteristics of ZnS-Sb@C@rGO.

form Zn and $NaZn_{13}$, respectively.[44] The two weak peaks at 0.75 and 1 V when the battery is charged belong to the dealloying procedure of Na_3Sb and $NaZn_{13}$.[45] Compared with Figure S6a,b in the Supporting Information, the overlap of the CV curves of the ZnS-Sb@C@rGO electrode is better than that of ZnS@C and ZnS-Sb@C, indicating that the ZnS-Sb@C@rGO electrode has better electrochemical reversibility. The specific reaction chemical equation of the ZnS-Sb@C@rGO composite is as follows:

$$ZnS + 2Na^+ + 2e^- \leftrightarrow Zn + Na_2S \quad (1)$$

$$13Zn + Na^+ + 3e^- \leftrightarrow 2Sb^o + 3NaZn_{13} \quad (2)$$

$$Sb^o + 3Na^+ + 3e^- \leftrightarrow Na_3Sb \quad (3)$$

In addition, galvanostatic charge−discharge curves (GCD) of the three samples were tested. In Figure S7a,b in the Supporting Information, the ZnS@C electrode's first-cycle charge−discharge specific capacities are 300.6 and 462.4 mAh g^{-1}, respectively. The first-cycle charge−discharge specific capacities of the ZnS-Sb@C electrode are 453.3 and 740.9 mAh g^{-1}, respectively, which suggests that the doped Sb brings some capacity to the battery. In Figure 4b, the charge−discharge capacities of the ZnS-Sb@C@rGO electrode in the first cycle are 584.9 and 903.6 mAh g^{-1}, respectively. Because the content of ZnS is the most abundant and the content of Sb is less in the sample, the GCD curves mainly show the charging and discharging voltage platforms of ZnS, and the charging and discharging voltage platforms of the three are generally similar. From the subsequent GCD curves, comparing with Figure S6a,b in the Supporting Information, ZnS-Sb@C@rGO shows that the voltage of the discharge platform is higher, the charging platform is gentler, and the GCD curves are highly overlapping, which show the best electrochemical reversibility and cycle stability. The high charge−discharge capacity of the ZnS-Sb@C@rGO electrode is attributed to the doping of the Sb element contributing part of the capacity, and the double coating of a carbon layer and rGO layer provides a good number of sodium embedding sites and transport channels for the composite material, enhancing the electrode reaction kinetics and electronic conductivity.[46,47]

Figure 4c gives the rate performance of different electrode materials. The discharge specific capacities of ZnS-Sb@C@rGO electrodes at 0.1, 0.2, 1, 2, and 3 A g^{-1} are 1117.1, 661.6,

https://doi.org/10.1021/acsanm.3c02158
ACS Appl. Nano Mater. 2023, 6, 13503−13512

448.7, 266.8, and 157.1 mAh g^{-1}, respectively, higher than the other two electrodes. When reduced back to 0.1 A g^{-1}, the discharge capacity of the ZnS-Sb@C@rGO electrode returns to 653.1 mAh g^{-1}. The discharge specific capacities of ZnS-Sb@C and ZnS@C only recovered to 462.1 and 340.6 mAh g^{-1}, showing that the composites supported by rGO and carbon layers exhibit a more outstanding rate performance. In Figure 4d, an obvious charge−discharge voltage plateau of ZnS-Sb@C@rGO is still observed at 3 A g^{-1}, which proves that it has good reaction kinetics. It shows a higher reversible capacity than the other two electrodes at different magnifications (Figure S8a,b). In Figure 4e, the ZnS-Sb@C@rGO has a reversible discharge capacity of 412 mAh g^{-1} after 100 cycles at 0.2 A g^{-1}, much higher than the two contrast electrodes. Figure 4f further shows the cycling ability of the ZnS-Sb@C@rGO electrode under a large current, and its reversible specific capacity is 210.3 mAh g^{-1} after 300 cycles under 1 A g^{-1}. The excellent cycle performance of the ZnS-Sb@C@rGO electrode is mainly due to the formation of a double-skeleton structure of rGO and carbon layers, which increases the electric conductivity of the composite material and provides buffer space for the sodification/desodification processes.

In Figure 4g,h, a galvanostatic intermittent titration technique (GITT) was used to further explore the kinetic advantages of ZnS-Sb@C@rGO. A pulse current of 100 mA g^{-1} was applied to the battery on the blue electric system for 600 s and then standing for 600 s. The specific calculation method of sodium ion diffusion coefficient is shown in formula (S1). Figure 4g,h shows the relationship between the Na^+ diffusion coefficient and potential of the three composites in the discharge−charging process. The ZnS-Sb@C@rGO electrode has a higher sodium ion diffusion coefficient at most potentials, which is related to the enhanced material conductivity of the carbon shell and rGO layer after coating. The Supporting Information shows the Na^+ diffusion coefficient of the ZnS-Sb@C@rGO electrode as a function of the open-circuit voltage (Figure S9a) and the GCD curves of the three electrodes during the initial cycle (Figure S9b−d). Figure 4i shows a before and after picture of two sodium half-cells connected in series to drive a small fan rotation with ZnS-Sb@C@rGO as the anode and a sodium sheet as the cathode.

The response kinetics of ZnS-Sb@C@rGO were analyzed by pseudocapacitive calculations. Figure 5a provides the CV curves of the ZnS-Sb@C@rGO electrode from 0.1 to 1 mV s^{-1}. As the sweep speed augments, oxidation peaks and reduction peaks move in opposite directions, and the general profiles are similar, indicating that the reaction process of the ZnS-Sb@C@rGO electrode involves both diffusion and capacitive behaviors.[48] The peak slope b value can be calculated by eq 4:[49]

$$\log i = b \log v + \log a \tag{4}$$

where a and b are variables. Diffusion control dominates when b is close to 0.5, and a capacitor control process dominates when b is close to 1. As shown in Figure 5b, b1 and b2 are both between 0.5 and 1, indicating that the ZnS-Sb@C@rGO electrode involves a mixed process of capacitive behavior and diffusion behavior during cycling. At a determined scanning speed, the capacitance contribution can also be quantitatively analyzed by eq 5[50]

$$i = k_1 v + k_2 v^{1/2} \tag{5}$$

The reaction resistance of the three electrodes was further analyzed by an electrochemical impedance test (EIS) at 0.01−100 kHz. In Figure 5e, the Nyquist curve presents a combination of semicircle and straight line, corresponding to charge transfer resistance (R_{ct}) and impedance (Z_w), respectively. The R_{ct} of ZnS-Sb@C@rGO before cycling is 271.1 Ω, which is less than the 401.2 Ω of ZnS@C, indicating that the doping of Sb and rGO improves the conductivity of the working electrode. Figure 5f shows that the σ values of ZnS@C, ZnS-Sb@C, and ZnS-Sb@C@rGO are 443.7, 277.5 and 268.7 Ω cm^2 $s^{-1/2}$, respectively. The Na^+ diffusion rate (D_{Na}) of each electrode is calculated as follows,[51] where the smaller the value of σ, the larger the value of D_{Na}.

$$D_{Na} = \frac{R^2T^2}{2A^2n^4F^4C^2\sigma^2} \tag{6}$$

R and T are the gas constants and temperatures in Kelvin, respectively. A and n are the surface area of the electrode and the number of electrons per unit mass. F, C, and σ represent the Faraday's constant, sodium ion concentration, and Warburg factor, respectively. Combined with Table S1, the specific value of the Na^+ diffusion rate of the ZnS-Sb@C@rGO electrode is 9.04×10^{-13} cm^2 s^{-1}, which is greater than those of the ZnS-Sb@C electrode (8.48×10^{-13} cm^2 s^{-1}) and ZnS-C electrode (3.32×10^{-13} cm^2 s^{-1}), which proves that ZnS-Sb@C@rGO has fast ion transfer kinetics. The main reason is that the conductive framework of rGO provides abundant 3D transfer channels for Na^+ deintercalation. Figure 5g shows the EIS spectrum of the three working electrodes after 100 cycles at 0.2 A g^{-1}. After cycling, the charge transfer resistance R_{ct} of the three electrodes increases, indicating that the Na^+ diffusion rate decreases. The ZnS-Sb@C@rGO electrode still shows the smallest resistance and the largest Na^+ diffusion rate compared with the ZnS-C and ZnS-Sb@C electrodes, indicating that the ZnS-Sb@C@rGO electrode has excellent electrical conductivity and charge transfer kinetics.

Figure 5h reveals the nature of sodium storage in ZnS-Sb@C@rGO composites. First, the mesoporous ZnS-Sb heterostructure core is designed with a synergistic effect, which increases the Na^+ transmission channel and electrode/electrolyte contact area. A heterogeneous electric field is formed between the two, which accelerates Na^+ transformation kinetics. Second, the double coating of the outer carbon shell and graphene layer provides plenty of Na^+ embedded sodium sites and overall improves the charge conversion kinetics of the composite. Finally, the unique design of the hierarchical core−shell heterostructure provides a buffer against the volume expansion during sodification/desodification..

As can be seen from the SEM image of ZnS-Sb@C@rGO after cycling in Figure S10a,b in the Supporting Information, ZnS-Sb@C@rGO still shows the shape of nanospheres with a loose and porous surface. Long-term cycling results in the loss of the outer rGO layer, but some carbon shells can still be observed embedded on the surface of the nanosphere. The results show that ZnS-Sb@C@rGO core−shell nanospheres have excellent structural durability. Compared with other Sb-based and Zn-based materials in Table S2, ZnS-Sb@C@rGO samples exhibit a very competitive cycling performance and Coulombic efficiency (99%, Figure 4e). The excellent electrochemical performance is due to the new design of the layered structure, which accelerates the Na^+ transfer and improves the transfer kinetics and structural stability of the electrode material.

https://doi.org/10.1021/acsanm.3c02158
ACS Appl. Nano Mater. 2023, 6, 13503−13512

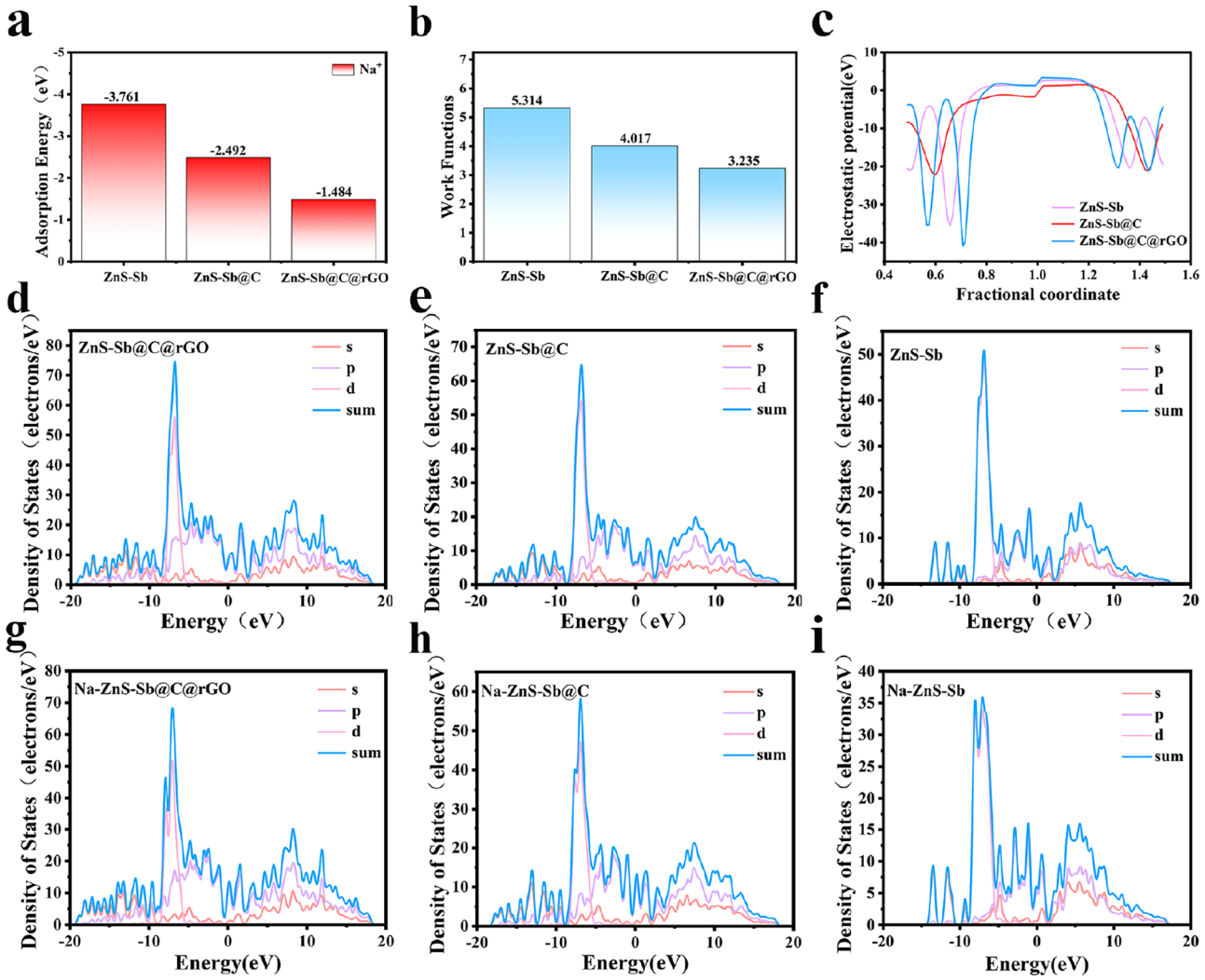

Figure 6. (a) Adsorption energy of sodium ions. (b) Function of power. (c) Substance work function potential diagram. Projected density of states (PDOS) for (d) ZnS-Sb@C@rGO, (e) ZnS-Sb@C, (f) ZnS-Sb, (g) Na-ZnS-Sb@C@rGO, (j) Na-ZnS-Sb@C, and (i) Na-ZnS-Sb.

Density functional theory (DFT) calculation was carried out to better explain the operating mechanism of the battery and the process of Na^+ ejection and insertion. Figure 6a shows the calculation of adsorption energy for Na^+ by Materials Studio. ZnS-Sb@C@rGO has an adsorption energy of −1.484 eV for Na^+, and ZnS-Sb@C has an adsorption energy of −2.492 eV for Na^+. The adsorption energy of ZnS-Sb for Na^+ is −3.761 eV. The huge interaction force between pure ZnS-Sb and Na makes Na^+ firmly embedded in the ZnS-Sb lattice, which is difficult to precipitate during discharge, resulting in a low Coulombic efficiency. After the introduction of C and rGO on the basis ZnS-Sb, the adsorption capacity of Na^+ is decreased successively, which is conducive to the adsorption and desorption of Na^+ and improves the reaction reversibility and cycle stability of the composite. Figure 6b,c shows the energy that electrons need to overcome when they transition from the inside of the material to its surface, known as the work function. The work function of the anode material in the sodium battery will directly affect the exchange reaction rate with sodium ions and the battery output voltage and also the durability and life of the anode material. The work function of ZnS-Sb@C@rGO is 3.235 eV, the work function of ZnS-Sb@C is 4.017 eV, and the work function of ZnS-Sb is 5.314 eV. The lower the work function, the less the energy required for Na^+ to migrate from the material, and the surface of the negative material can interact with Na^+ more easily. ZnS-Sb@C@rGO has a smaller work function to provide a better electrochemical performance. In Figure 6c, it can be seen that the introduction of rGO and C reduced the electrostatic potential, thus changing the work function, reducing the energy required for the escape of electrons on the surface of the material, and enhancing the conversion of Na^+ with the anode electrode material. Figure S11 shows the molecular model diagram and three-dimensional charge-difference density diagram of Na-ZnS-Sb, Na-ZnS-Sb@C, and Na-ZnS-Sb@C@rGO, where blue indicates the increase of electron density and yellow indicates the decrease of electron density. The blue areas are denser and have a denser electron density, while the yellow areas are less dense and have less electron density. After the slice is observed, the red region gains electrons and the blue region loses electrons.

Figure 6d−i shows the track distribution of PDOS. The higher the material state density of the anode electrode of the battery, the higher the stored electricity and the higher the battery energy density. Compared with ZnS-Sb@C and ZnS-Sb, the ZnS-Sb@C@rGO anode material has a higher state density and higher energy density, which make the battery have a higher sodium storage capacity. After entering the

https://doi.org/10.1021/acsanm.3c02158
ACS Appl. Nano Mater. 2023, 6, 13503−13512

anode material through electron transmission, Na^+ forms an energy storage state, and the s orbital, p orbital, and d orbital change in the system. It can be seen that Na^+ is stored in the s orbital, p orbital, and d orbital of the anode material. Compared with Na-ZnS-Sb@C and Na-ZnS-Sb, the orbital states of Na-ZnS-Sb@C@rGO composites have higher densities, which may be due to the introduction of C and rGO, resulting in a large number of loose electron clouds in the s, p and d orbital hybrids of anode materials, which can effectively transport electrons. The adsorption of Na^+ fills the band gap at the top of the valence band and the bottom of the conduction band and improves the conductivity of the composite.

4. CONCLUSIONS

In this paper, we designed a unique ZnS-Sb@C@rGO core−shell nanospheres by using a ZnS nanosphere as a template. The ZnS-Sb heterogeneous core can accelerate Na^+/electron transfer, increase electrolyte/electrode contact area, and improve material conversion kinetics. Meanwhile, the rGO and carbon layers are uniformly covered on the surface of the ZnS-Sb nanosphere to form a three-dimensional conductive skeleton structure. This framework improves the conductivity of the working electrode, provides a rich buffer space for the working electrode during the sodiumation/desodiumation process, and extends the cycle life of the electrode. The ZnS-Sb@C@rGO composite was further applied to rotate a small fan in the sodium half battery. The SEM images after subsequent cycling further confirmed that the synergistic effect of the ZnS-Sb core and the outer double carbon layer can effectively improve the pulverization and collapse of electrode materials. The synthetic ZnS-Sb@C@rGO core−shell nanopheres have an impressive structural durability. Therefore, the unique ZnS-Sb@C@rGO core−shell nanopheres can be used as a significant means to improve the energy storage of SIBs.

■ ASSOCIATED CONTENT

Supporting Information

The Supporting Information is available free of charge at https://pubs.acs.org/doi/10.1021/acsanm.3c02158.

SEM images and TEM images of the sample under different magnifications; EDX image; TGA image; Raman image; CV curves and GCD curves of the control sample; GCD curves of the control sample under the current density; GITT tests of the GCD curves of each sample in the initial cycle; SEM images after circulation; DFT calculation of the differential charge density of the sample; electrode kinetic parameters of the three samples; and electrochemical properties of the experimental results compared with other reported experimental results (PDF)

■ AUTHOR INFORMATION

Corresponding Authors

Liying Wang − *Key Laboratory of Advanced Structural Materials, Ministry of Education & Advanced Institute of Materials Science, Changchun University of Technology, Changchun 130012, China;* orcid.org/0000-0002-7399-8698; Phone: +86-0431-85716421; Email: wangliying@ccut.edu.cn; Fax: +86-0431-85716426

Wei Lü − *Key Laboratory of Advanced Structural Materials, Ministry of Education & Advanced Institute of Materials Science, Changchun University of Technology, Changchun 130012, China; State Key Laboratory of Luminescence and Applications, Changchun Institute of Optics, Fine Mechanics and Physics, Chinese Academy of Sciences, Changchun 130033, China;* orcid.org/0000-0002-7070-8456; Phone: +86-0431-85716421; Email: lw771119@hotmail.com; Fax: +86-0431-85716426

Authors

Ming Zhu − *Key Laboratory of Advanced Structural Materials, Ministry of Education & Advanced Institute of Materials Science, Changchun University of Technology, Changchun 130012, China*

Yi Jiang − *School of Science, Changchun Institute of Technology, Changchun 130012, China;* orcid.org/0000-0003-3401-6986

Xijia Yang − *Key Laboratory of Advanced Structural Materials, Ministry of Education & Advanced Institute of Materials Science, Changchun University of Technology, Changchun 130012, China;* orcid.org/0000-0001-9424-3596

Xuesong Li − *Key Laboratory of Advanced Structural Materials, Ministry of Education & Advanced Institute of Materials Science, Changchun University of Technology, Changchun 130012, China*

Complete contact information is available at: https://pubs.acs.org/10.1021/acsanm.3c02158

Author Contributions

M.Z.: conceptualization, writing−original draft. Y.J.: formal analysis. X.Y.: resources. X.L.: validation, investigation. L.W.: supervision. W.L.: writing−review & editing.

Notes

The authors declare no competing financial interest.

■ ACKNOWLEDGMENTS

This work was supported by the Department of Science and Technology of Jilin Province (grant nos. 20210101077JC, YDZJ202201ZYTS361, 20230101330JC, and 20220101235JC) and the National Natural Science Foundation of China (grant nos. 62004014 and 62004015).

■ REFERENCES

(1) Costa, C. M.; Barbosa, J. C.; Gonçalves, R.; Castro, H.; Campo, F. J. D.; Lanceros-Méndez, S. Recycling and environmental issues of lithium-ion batteries: Advances, challenges and opportunities. *Energy Storage Mater.* **2021**, *37*, 433−465.

(2) Du, Y.; Yi, Z.; Chen, B.; Xu, J.; Zhang, Z.; Bao, J.; Zhou, X. Sn_4P_3 nanoparticles confined in multilayer graphene sheets as a high-performance anode material for potassium-ion batteries. *J. Energy Chem.* **2022**, *66*, 413−421.

(3) Du, Y.; Zhang, Z.; Xu, Y.; Bao, J.; Zhou, X. Metal Sulfide-Based Potassium-Ion Battery Anodes: Storage Mechanisms and Synthesis Strategies. *Acta Phys.-Chim. Sin.* **2022**, *0*, 2205017.

(4) Di Lecce, D.; Verrelli, R.; Hassoun, J. Lithium-ion batteries for sustainable energy storage: recent advances towards new cell configurations. *Green Chem.* **2017**, *19*, 3442−3467.

(5) Fu, L.; Shang, C.; Li, G.; Hu, L.; Zhang, X.; Huang, L.; Wang, X.; Zhou, G. Lithium Pre-cycling Induced Fast Kinetics of Commercial Sb_2S_3 Anode for Advanced Sodium Storage. *Energy Environ. Mater.* **2019**, *2*, 209−215.

(6) Zhou, X.; Wan, L. J.; Guo, Y. G. Binding SnO_2 nanocrystals in nitrogen-doped graphene sheets as anode materials for lithium-ion batteries. *Adv. Mater.* **2013**, *25*, 2152−2157.

(7) Ding, X.; Shao, J.; Lv, L.; Zhu, Y.; Jiang, Y.; Shi, Q.; Qu, Q.; Zheng, H. Yolk-Shell Sb_2S_3@C Hollow Microspheres with Controllable Interiors for High Space Utilization and Structural Stability of Na-Storage. *ChemNanoMat* **2022**, *8*, No. e202100515.
(8) Xu, J.; Xu, Y.; Lai, C.; Xia, T.; Zhang, B.; Zhou, X. Challenges and perspectives of covalent organic frameworks for advanced alkali-metal ion batteries. *Sci. China Chem.* **2021**, *64*, 1267−1282.
(9) Li, J.; Li, Z.; Tang, S.; Hao, J.; Wang, T.; Wang, C.; Pan, L. Improving the sodium storage performance of carbonaceous anode: Synergistic coupling of pore structure and ordered domain engineering. *Carbon* **2023**, *203*, 469−478.
(10) Abraham, K. M. How Comparable Are Sodium-Ion Batteries to Lithium-Ion Counterparts. *ACS Energy Lett.* **2020**, *5*, 3544−3547.
(11) Li, J.; Li, Z.; Tang, S.; Wang, T.; Wang, K.; Pan, L.; Wang, C. Sodium titanium phosphate nanocube decorated on tablet-like carbon for robust sodium storage performance at low temperature. *J. Colloid Interface Sci.* **2022**, *629*, 121−132.
(12) Kim, S.-W.; Seo, D.-H.; Ma, X.; Ceder, G.; Kang, K. Electrode Materials for Rechargeable Sodium-Ion Batteries: Potential Alternatives to Current Lithium-Ion Batteries. *Adv. Energy Mater.* **2012**, *2*, 710−721.
(13) Zhao, W.; Yuan, S.; Lei, S.; Zeng, Z.; Dong, J.; Jiang, F.; Yang, Y.; Sun, W.; Ji, X.; Ge, P. Tailoring Rational Crystal Orientation and Tunable Sulfur Vacancy on Metal-Sulfides toward Advanced Ultrafast Ion-Storage Capability. *Adv. Funct. Mater.* **2022**, *33*, No. 2211542.
(14) Wong, D. P.; Suriyaprabha, R.; Yuvakumar, R.; Rajendran, V.; Chen, Y.-T.; Hwang, B.-J.; Chen, L.-C.; Chen, K.-H. Binder-free rice husk-based silicon−graphene composite as energy efficient Li-ion battery anodes. *J. Mater. Chem. A* **2014**, *2*, 13437−13441.
(15) Ge, P.; Zhang, L.; Zhao, W.; Yang, Y.; Sun, W.; Ji, X. Interfacial Bonding of Metal-Sulfides with Double Carbon for Improving Reversibility of Advanced Alkali-Ion Batteries. *Adv. Funct. Mater.* **2020**, *30*, No. 1910599.
(16) Ni'mah, Y. L.; Cheng, M.-Y.; Cheng, J. H.; Rick, J.; Hwang, B.-J. Solid-state polymer nanocomposite electrolyte of TiO_2/PEO/$NaClO_4$ for sodium ion batteries. *J. Power Sources* **2015**, *278*, 375−381.
(17) Zhang, Y.; Li, J.; Ma, L.; Li, H.; Xu, X.; Liu, X.; Lu, T.; Pan, L. Insights into the storage mechanism of 3D nanoflower-like V_3S_4 anode in sodium-ion batteries. *Chem. Eng. J.* **2022**, *427*, No. 130936.
(18) Cao, L.; Gao, X.; Zhang, B.; Ou, X.; Zhang, J.; Luo, W.-B. Bimetallic Sulfide Sb_2S_3@FeS_2 Hollow Nanorods as High-Performance Anode Materials for Sodium-Ion Batteries. *ACS Nano* **2020**, *14*, 3610−3620.
(19) Yuan, S.; Zhao, W.; Zeng, Z.; Dong, Y.; Yang, Y.; Sun, W.; Ge, P. Engineering hierarchical Sb_2S_3/N−C from natural minerals with stable phase-change towards all-climate energy storage. *J. Mater. Chem. A* **2022**, *10*, 5488−5504.
(20) Qin, W.; Li, D.; Zhang, X.; Yan, D.; Hu, B.; Pan, L. ZnS nanoparticles embedded in reduced graphene oxide as high performance anode material of sodium-ion batteries. *Electrochim. Acta* **2016**, *191*, 435−443.
(21) Hou, H.; Jing, M.; Huang, Z.; Yang, Y.; Zhang, Y.; Chen, J.; Wu, Z.; Ji, X. One-Dimensional Rod-Like Sb_2S_3-Based Anode for High-Performance Sodium-Ion Batteries. *ACS Appl. Mater. Interfaces* **2015**, *7*, 19362−19369.
(22) Song, Z.; Wang, G.; Chen, Y.; Chang, Q.; Lu, Y.; Wen, Z. Construction of hierarchical NiS@C/rGO heterostructures for enhanced sodium storage. *Chem. Eng. J.* **2022**, *435*, No. 134633.
(23) Zhang, G.; Wei, S.; Belcher, A. M. Biotemplated Zinc Sulfide Nanofibers as Anode Materials for Sodium-Ion Batteries. *ACS Appl. Nano Mater.* **2018**, *1*, 5631−5639.
(24) Pan, J.; Zuo, Z.; Deng, J.; Yao, Q.; Wang, Z.; Zhou, H. Sb_2S_3 single crystal nanowires with comparable electrochemical properties as an anode for sodium ion batteries. *Surf. Interfaces* **2018**, *10*, 170−175.
(25) Jing, W. T.; Zhang, Y.; Gu, Y.; Zhu, Y. F.; Yang, C. C.; Jiang, Q. N-Doped Carbon Nanonecklaces with Encapsulated Sb as a Sodium-Ion Battery Anode. *Matter* **2019**, *1*, 720−733.
(26) Hou, H.; Jing, M.; Zhang, Y.; Chen, J.; Huang, Z.; Ji, X. Cypress leaf-like Sb as anode material for high-performance sodium-ion batteries. *J. Mater. Chem. A* **2015**, *3*, 17549−17552.
(27) Hou, H.; Jing, M.; Yang, Y.; Zhang, Y.; Zhu, Y.; Song, W.; Yang, X.; Ji, X. Sb porous hollow microspheres as advanced anode materials for sodium-ion batteries. *J. Mater. Chem. A* **2015**, *3*, 2971−2977.
(28) Pan, Z.; Qin, T.; Zhang, W.; Chu, X.; Dong, T.; Yue, N.; Wang, Z.; Zheng, W. Non-layer-transformed Mn_3O_4 cathode unlocks optimal aqueous magnesium-ion storage via synergizing amorphous ion channels and grain refinement. *J. Energy Chem.* **2022**, *68*, 42−48.
(29) Zhao, Z.; Zhang, W.; Liu, M.; Yoo, S. J.; Yue, N.; Liu, F.; Zhou, X.; Song, K.; Kim, J. G.; Chen, Z.; Lang, X. Y.; Jiang, Q.; Zhi, C.; Zheng, W. Ultrafast Nucleation Reverses Dissolution of Transition Metal Ions for Robust Aqueous Batteries. *Nano Lett.* **2023**, *23*, 5307−5316.
(30) Xiang, Y.; Li, Q.; Wei, X.; Li, X.; Zheng, Q.; Huo, Y.; Lin, D. Constructing NiS_2/$NiSe_2$ heteroboxes with phase boundaries for Sodium-Ion batteries. *J. Colloid Interface Sci.* **2022**, *607*, 752−759.
(31) Wang, L.; Li, D.; Li, Q.; Pan, Q.; Zhang, M.; Zhang, L.; Zheng, F.; Huang, Y.; Wang, H.; Li, Q. Ultrafine ZnS nanoparticles embedded in N-doped carbon as advanced anode materials for lithium ion batteries and sodium ion batteries. *J. Alloys Compd.* **2022**, *910*, No. 164783.
(32) Yang, J.; Li, J.; Wang, T.; Notten, P. H. L.; Ma, H.; Liu, Z.; Wang, C.; Wang, G. Novel hybrid of amorphous Sb/N-doped layered carbon for high-performance sodium-ion batteries. *Chem. Eng. J.* **2021**, *407*, No. 127169.
(33) Du, X.; Zhao, H.; Lu, Y.; Zhang, Z.; Kulka, A.; Świerczek, K. Synthesis of core-shell-like ZnS/C nanocomposite as improved anode material for lithium ion batteries. *Electrochim. Acta* **2017**, *228*, 100−106.
(34) Liu, J.; Yu, L.; Wu, C.; Wen, Y.; Yin, K.; Chiang, F. K.; Hu, R.; Liu, J.; Sun, L.; Gu, L.; Maier, J.; Yu, Y.; Zhu, M. New Nanoconfined Galvanic Replacement Synthesis of Hollow Sb@C Yolk-Shell Spheres Constituting a Stable Anode for High-Rate Li/Na-Ion Batteries. *Nano Lett.* **2017**, *17*, 2034−2042.
(35) Wang, H.; Song, X.; Lv, M.; Jin, S.; Xu, J.; Kong, X.; Li, X.; Liu, Z.; Chang, X.; Sun, W.; Zheng, J.; Li, X. Interfacial Covalent Bonding Endowing Ti_3C_2-Sb_2S_3 Composites High Sodium Storage Performance. *Small* **2022**, *18*, No. e2104293.
(36) Zhang, Y.-h.; Wang, D.-d.; Yan, H.-y.; Liu, R.-h.; Yang, D.; Yu, S.-h.; Luo, S.-h.; Wang, Q.; Liu, X. One-pot method synthesis of the multi-morphology Sb_2S_3 superstructure increasing the sodium storage capacity and expanding the interlayer spacing. *Appl. Surf. Sci.* **2022**, *591*, No. 153138.
(37) Zhan, W.; Zhu, M.; Lan, J.; Wang, H.; Yuan, H.; Yang, X.; Sui, G. 1D Sb_2S_3@nitrogen-doped carbon coaxial nanotubes uniformly encapsulated within 3D porous graphene aerogel for fast and stable sodium storage. *Chem. Eng. J.* **2021**, *408*, No. 128007.
(38) Ai, J.; Zhao, X.; Lei, Y.; Yang, S.; Xu, Q.; Lai, C.; Peng, C. Pomegranate-inspired SnS/ZnS@C heterostructural nanocubes towards high-performance sodium ion battery. *Appl. Surf. Sci.* **2019**, *496*, No. 143631.
(39) Li, X.; Liang, H.; Liu, X.; Sun, R.; Qin, Z.; Fan, H.; Zhang, Y. Ion-exchange strategy of CoS_2/Sb_2S_3 hetero-structured nanocrystals encapsulated into 3D interpenetrating dual-carbon framework for high-performance Na^+/K^+ batteries. *Chem. Eng. J.* **2021**, *425*, No. 130657.
(40) Liu, J.; Xu, Y.-G.; Kong, L.-B. Synthesis of high-performance Mo_2S_3/NiS_2-RGO anode materials and its applications in sodium-ion batteries and sodium-ion capacitors. *Ionics* **2020**, *26*, 4499−4510.
(41) Zhang, G.; Zeng, S.; Duan, L.; Zhang, X.; Wang, L.; Yang, X.; Li, X.; Lü, W. The Dual Capacity Contribution Mechanism of SnSb-Anchored Nitrogen-Doped 3D Reduced Graphene Oxide Enhances the Performance of Sodium-Ion Batteries. *ChemElectroChem* **2020**, *7*, 4663−4671.
(42) Zhao, J.; Zhu, M.; Pang, Y.; Wu, H.; Ding, S. Layered NiPS3 nanoparticles anchored on two-dimensional nitrogen-doped biochar

https://doi.org/10.1021/acsanm.3c02158
ACS Appl. Nano Mater. 2023, 6, 13503−13512

nanosheets for ultra-high rate sodium-ion storage. *Compos. Commun.* **2022**, *29*, No. 100988.
(43) Yu, S.; Zhang, X.; Zhang, P. Prediction of New Structures of the Na-Sb Alloy Anode for Na-Ion Batteries. *J. Phys. Chem. C* **2022**, *126*, 11468−11474.
(44) Dong, S.; Li, C.; Ge, X.; Li, Z.; Miao, X.; Yin, L. ZnS-Sb_2S_3@C Core-Double Shell Polyhedron Structure Derived from Metal-Organic Framework as Anodes for High Performance Sodium Ion Batteries. *ACS Nano* **2017**, *11*, 6474−6482.
(45) Dong, S.; Li, C.; Li, Z.; Zhang, L.; Yin, L. Mesoporous Hollow Sb/ZnS@C Core-Shell Heterostructures as Anodes for High-Performance Sodium-Ion Batteries. *Small* **2018**, *14*, No. 1704517.
(46) Li, Q.; Zhang, W.; Peng, J.; Zhang, W.; Liang, Z.; Wu, J.; Feng, J.; Li, H.; Huang, S. Metal-Organic Framework Derived Ultrafine Sb@Porous Carbon Octahedron via In Situ Substitution for High-Performance Sodium-Ion Batteries. *ACS Nano* **2021**, *15*, 15104−15113.
(47) Zhang, W.; Liu, Y.; Chen, C.; Li, Z.; Huang, Y.; Hu, X. Flexible and Binder-Free Electrodes of Sb/rGO and $Na_3V_2(PO_4)_3$/rGO Nanocomposites for Sodium-Ion Batteries. *Small* **2015**, *11*, 3822−3829.
(48) Zhao, D.; Zhang, Z.; Ren, J.; Xu, Y.; Xu, X.; Zhou, J.; Gao, F.; Tang, H.; Liu, S.; Wang, Z.; Wang, D.; Wu, Y.; Liu, X.; Zhang, Y. Fe_2VO_4 nanoparticles on rGO as anode material for high-rate and durable lithium and sodium ion batteries. *Chem. Eng. J.* **2023**, *451*, No. 138882.
(49) Nguyen, A.-G.; Le, H. T. T.; Verma, R.; Vu, D.-L.; Park, C.-J. Boosting sodium-ion battery performance using an antimony nanoparticle self-embedded in a 3D nitrogen-doped carbon framework anode. *Chem. Eng. J.* **2022**, *429*, No. 132359.
(50) Zhang, P.; Zhu, Q.; Wei, Y.; Xu, B. Achieving stable and fast potassium storage of Sb_2S_3@MXene anode via interfacial bonding and electrolyte chemistry. *Chem. Eng. J.* **2023**, *451*, No. 138891.
(51) Ma, W.; Wang, J.; Gao, H.; Niu, J.; Luo, F.; Peng, Z.; Zhang, Z. A mesoporous antimony-based nanocomposite for advanced sodium ion batteries. *Energy Storage Mater.* **2018**, *13*, 247−256.

https://doi.org/10.1021/acsanm.3c02158
ACS Appl. Nano Mater. 2023, 6, 13503−13512